Deep–Sea Research II 209 (2023) 105298

Contents lists available at ScienceDirect

Deep-Sea Research Part II

journal homepage: www.elsevier.com/locate/dsr2

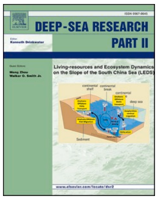

Causal relations between the loop current penetration and the inflow/outflow conditions inferred with a rigorous quantitative causality analysis

Yang Yang [a,*], Guanqi Fu [b], X. San Liang [c,d], Robert H. Weisberg [e], Yonggang Liu [e]

[a] *State Key Laboratory of Marine Environmental Science, College of Ocean and Earth Sciences, Xiamen University, Xiamen, China*
[b] *School of Marine Sciences, Nanjing University of Information Science and Technology, Nanjing, China*
[c] *Department of Atmospheric and Oceanic Sciences, And Institute of Atmospheric Sciences, Fudan University, Shanghai, China*
[d] *The Artificial Intelligence Group, Division of Frontier Research, Southern Marine Laboratory, Zhuhai, China*
[e] *College of Marine Science, University of South Florida, St. Petersburg, FL, USA*

ARTICLE INFO

Handling Editor: Dr. K Drinkwater

Keywords:
Loop current
Yucatan channel
Straits of Florida
Causality analysis

ABSTRACT

The causal relationship between the Loop Current (LC) penetration into the Gulf of Mexico and the inflow/outflow conditions in the Yucatan Channel and the Straits of Florida is analyzed using a recently developed causality analysis, which is quantitative in nature, and rigorously derived from first principles. Long-term time series from a 23-year high-resolution reanalysis product reveals that the LC penetration is associated with a dipole (tripole) mode of transport (vorticity flux) in both channels. These relationships, though significant from a perspective of correlation, do not necessarily imply causality. By applying the causality analysis, we identify a clear asymmetry of causality, that is, the flow conditions in the Yucatan Channel and the Straits of Florida can both cause the LC penetration. Conversely, the LC path state is less causal to the current variability in the two channels. The spatial causal structures further reveal that the upstream influence from the Yucatan Channel is strong in the main body of the LC as well as its extension area, while the downstream influence from the Straits of Florida is confined within the eastern branch of the LC. The asymmetric causal relations obtained from the data-assimilative reanalysis product are further confirmed in a free-running model simulation forced by three repeated cycles of atmospheric forcing, although the strength of the causality could vary from one simulation cycle to another, due to the intrinsic variability of the LC system.

1. Introduction

The Loop Current (LC) is the dominant driver of circulation in the Gulf of Mexico (GoM). It enters the GoM through the Yucatan Channel (YC), forms an anticyclonic loop, and exits through the Straits of Florida (FS). The LC is known for its bimodal path oscillation between an extended and a retracted state. During the extended state, the LC takes a northward detoured path, while in the retracted state, the LC flows close along the northwest coast of Cuba (Fig. 1). Northward penetration of the LC is usually followed by the detachment of an anticyclonic eddy from the parent LC. A rich literature now exists addressing the mechanisms that control the penetration of LC and its associated eddy shedding processes (e.g., National Academies of Sciences, E., 2018). It has been well recognized that most of the eddy shedding events are preceded by mesoscale cyclonic eddies/meanders that cut through the extended LC (e.g., Schmitz, 2005; Chérubin et al., 2006; Rudnick et al., 2014; Donohue et al., 2016; Hamilton et al., 2016; Nickerson et al., 2022). Satellite observation shows that mesoscale perturbations are more likely to evolve into coherent structures on the eastern side of the LC (see Fig. 1a) due to strong energy transfers via baroclinic instability (Donohue et al., 2016; Xu et al., 2013). A recent study also found that barotropic instability is responsible to initiate cyclonic perturbations on the western side of the LC as they are advected downstream to the northeast in deep water and experience another major growth interval by baroclinic instability, leading to eddy shedding and possible LC retraction (Yang et al., 2020). Nickerson et al. (2022) showed that there is an ordered sequence of behaviors as the LC evolves through its extended, retracted and eddy shedding states and that transition to the retracted state requires cyclonic eddies pinching from both the east and west sufficiently far south to enable the LC to detach from the Yucatan escarpment.

Unlike the eddy shedding phenomenon, the penetration of the LC

---

* Corresponding author.
E-mail address: yangyangoceano@gmail.com (Y. Yang).

https://doi.org/10.1016/j.dsr2.2023.105298
Received 12 November 2022; Received in revised form 8 May 2023; Accepted 9 May 2023

into the GoM, which is a precursor to eddy shedding process, is less understood. Up to now, it remains unknown whether the highly irregular fluctuation of the LC path state is more intrinsic or externally forced. Lugo-Fernández (2007) investigated the intrinsic property of the LC and suggested that the LC is not entirely chaotic but behaves as a nonlinear oscillator with limited predictability. On the other hand, many researchers have focused on the connection between the LC behavior and external factors such as inflow conditions at the YC (e.g., Bunge et al., 2002; Candela et al., 2002; Ezer et al., 2003; Oey, 2004; Nedbor-Gross et al., 2014; Huang et al., 2021), outflow fluctuations at the FS (e.g., Sturges et al., 2010; Mildner et al., 2013), wind forcing (e.g., Y.-L. Chang and Oey, 2013), and topographic anchoring (Weisberg and Liu, 2017). Among these external factors, the temporal changes of the transport and vorticity flux at the entry and exit channels and their relations with the LC path state have attracted considerable attention. Intuitively, by the mass conservation principle, the LC tends to penetrate northward when the inflow transport through the YC exceeds the outflow transport through the FS. This simple relation, as first suggested by Maul (1977), however, does not seem to hold according to early measurements (Maul et al., 1985; Maul and Vukovich, 1993). Later, Bunge et al. (2002) analyzed a 9-month record (September 1999–June 2000) from the CANEK observation program (Sheinbaum et al., 2002) and found a significant correlation between the LC path and the deep transport in the YC, the later of which is interpreted as the compensation of the mass imbalance between the upper YC and the FS and is found to lag behind the LC path variation by about one week.

In the past two decades, the advent of high-resolution satellite measurements and long-record *in situ* observations have provided robust information about the relation between the LC path variation and the transports through the two channels. Several observation-based studies have found that extension (retraction) of the LC leads to lower (higher) transports through both the YC and the FS (Alvera-Azcárate et al., 2009; Hirschi et al., 2019; Sheinbaum et al., 2002). Two modelling studies confirmed this relation but proposed different mechanisms (Lin et al., 2009; Mildner et al., 2013). Lin et al. (2009) argued that the transport strengths across the two channels are influenced by the changes in density and pressure anomaly in response to the interaction between the LC and variable bottom topography. In contrast, Mildner et al. (2013) provided a simpler explanation that the existence of a coherent eddy within the LC during the extended state partly blocks the inflow through YC and hence lead to a decrease of the outflow. Numerical results of Chang and Oey (2013) suggested that strong easterlies over the Caribbean Sea enhances the Yucatan transport which leads to northward extension of the LC. This contrasts with Lin et al. (2009) and Mildner et al. (2013) results. Recently, Athié et al. (2019) revisited Chang and Oey (2013)'s idea and found no such clear connection between the wind forcing, Yucatan transport and LC behavior in the long-term mooring and satellite altimetry records.

Besides transport, another group of studies tried to establish a causal relation between the vorticity flux through the YC and the LC penetration (Candela et al., 2002; Hurlburt and Thompson, 1980; Oey, 2004; Oey et al., 2003; Sheinbaum et al., 2016). However, the correspondence between the LC path and the vorticity influx seems even more complex and contradicting views exist in literature. Based on two-year-long mooring records from the CANEK program, Candela et al. (2002) found that periods of cumulative negative (anticyclonic) vorticity influx are related to LC expansion, while those of cumulative positive (cyclonic) vorticity influx are related to the retraction and eddy shedding of the LC. In contrast, Oey (2004) analyzed the same dataset and suggested that positive (cyclonic) vorticity tends to extend the LC into the GoM, while retraction or eddy shedding events are more likely to occur at times of negative (anticyclonic) vorticity influx. The reason for this disagreement, as also explained by Oey (2004), is that the relationship between the LC behavior and the vorticity influx is variable and no statistically robust conclusion can be made from the short observation records. Another problematic issue should also be mentioned. The vorticity flux is maximized and reverses signs along a very narrow band at the western side of the YC. The resolution of the CANEK observation is too sparse (only 2–3 moorings in the western side of the channel) to sufficiently capture the variable horizontal structure of the vorticity influx. Recently, Lugo-Fernández (2023) integrated the shallow water equations in an idealized setting and found that the time rate of change of the LC area is proportional to the reduction of kinetic energy across the LC which can be induced by the vorticity influx at the YC, even with a constant YC transport. The above results from previous studies suggest that even though vorticity is the horizontal derivative of the velocity, the influences of these two variables on the LC penetration may be dynamically different. Therefore, both will be chosen as the indices of inflow and outflow conditions of the LC in the present study.

Detecting the causality between time series has been a notorious challenge in scientific research (e.g., Imbens and Rubin, 2015; Liang, 2014, 2021). In this study, we seek to use a novel causal inference formalism to quantify the complex causal-effect relations between the LC path variation and the inflow/outflow conditions. The new method is based on the theory of information flow (IF), a fundamental physical concept associated with causality that has just been put on a rigorous footing, and formulated from first principles (Liang, 2008, 2014, 2016, 2021). Different from other existing statistical formalisms, the IF-based causality analysis provides both the direction as well as the magnitude of the causality between variables. We make use of the 1/12.5° data-assimilative reanalysis product of the Hybrid Coordinate Ocean Model (HYCOM) and a 1/25° free running multidecadal (54 years) simulation of HYCOM to perform this analysis. The rest of the paper is organized as follows: We describe the data and IF-based causality method in section 2, present the major results in sections 3, and give a summary in section 4.

2. Data and method

2.1. Data

Due to the limited spatial and temporal coverage of *in situ*

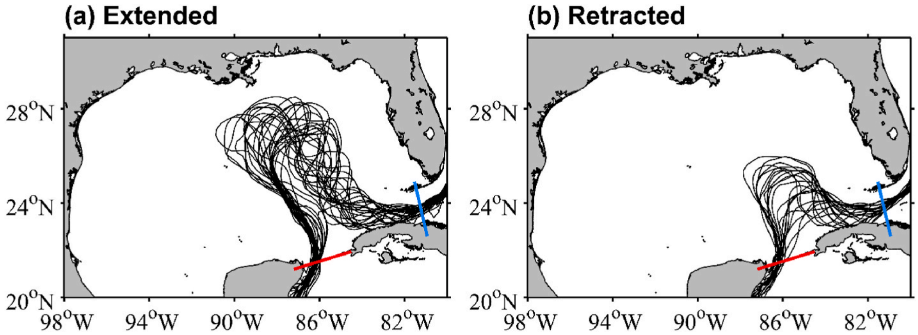

Fig. 1. Paths of the LC axis defined by the 0.17-m contour in the daily altimetry SSH fields during (a) the extended phase and (b) the retracted phase. The steric part of the SSH, which is the area mean of the SSH over the GoM, is removed before the calculation. The dates of each phase are marked in Fig. 2. Note that the dates chosen for the extended phase are taken when the LC (particularly the east side) has substantial meander activity. Red and blue lines indicate the cross sections where the model data are extracted in the Yucatan Channel and the Straits of Florida, respectively.

observations, daily outputs of the 1/12.5° HYCOM reanalysis product from 1994 to 2016 are used in this study. The HYCOM uses the Navy Coupled Ocean Data Assimilation (NCODA) system (Cummings, 2005) to assimilate available satellite sea surface height (SSH) and sea surface temperature, *in situ* vertical profiles of temperature and salinity from moored buoys, XBTs and Argo floats (Helber et al., 2013). Previous model-observation comparisons indicate that the HYCOM + NCODA system has a good performance in reproducing the observed features of the LC as well as inflow/outflow variabilities (Rosburg et al., 2016; Rousset and Beal, 2011). Fig. 2 compares the time series of the LC position, defined by the northernmost location of the 0.17-m SSH contour, in the altimetry observation (blue line) and the HYCOM reanalysis (red line). The correlation between the two time series is statistically significant over the 99% confidence level ($r = 0.82$), suggesting that the HYCOM well captures the observed LC path variation. The HYCOM results are also compared with the two-year-long YC transport series from the CANEK program (Candela et al., 2019) (Fig. 3). Note that both time series have been low-pass filtered by a cutoff period of 7 days as done in Candela et al. (2019). Despite some discrepancies in the high-frequency scale, the low-frequency trends of the transport series are similar in the HYCOM and CANEK observation. The correlation is 0.65 (statistically significant over the 99% confidence level) and reaches above 0.7 (statistically significant over the 90% confidence level) when a 30-day low-pass filtering is applied to both series. There exists another noticeable discrepancy between the mean transport in the HYCOM and CANEK. The observed mean transport during the considered period is 27.5 Sv, which is larger than that in the HYCOM (24.3 Sv). The HYCOM performance in the FS is similar to that in the YC (not shown). Transports through the YC and FS are found to be highly correlated (simultaneous correlation coefficient $r = 0.94$; statistically significant over the 99% confidence level) with no appreciable lag both in the observation (Candela et al., 2019) and the HYCOM reanalysis (see below). These results suggest that the HYCOM reanalysis produces a fairly realistic simulation of the LC system and hence is suitable for the purpose of this study.

To further add credibility to the results revealed in the data-assimilative HYCOM reanalysis, this study also uses data from a free running 54-year simulation of the HYCOM (Dukhovskoy et al., 2015). This multidecadal simulation has a horizontal resolution of 1/25°, configured in the domain from 18.9°N to 31.96°N and from 98°W to 76.4°W. The lateral boundary condition is provided by the bi-weekly climatological fields from a four-year (2000–2003) 1/12° degree North Atlantic HYCOM simulation, which is repeated each year. The model is initialized from another spin-up simulation from rest. The atmospheric forcing is obtained from the Climate Forecast System Reanalysis (CFSR) for 1992 to 2009. The 18-year record of atmospheric forcing is repeated three times, producing a continuous 54-year model solution. In this way, it provides us three realizations of the virtual ocean with different initial conditions. (Note that only the initial condition of the first 18-year cycle is prescribed. Those of the second and third cycles are generated by the simulation itself.) A more thorough description of the model configuration can be found online (https://www.hycom.org/data/goml0pt04/expt-02pt2). As this simulation is not constrained by data assimilation, the LC behavior in the simulation no longer matches the real ocean. With different initial conditions but identical lateral boundary and surface forcing, the three cycles of the model solution enable us to identify the effect of internal nonlinear dynamics on the casual relations between the LC path state and inflow/outflow conditions.

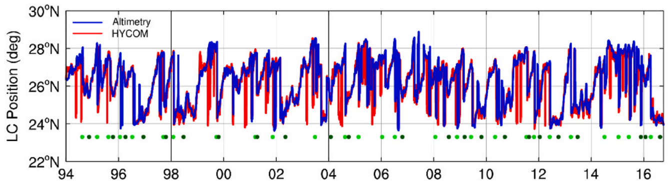

Fig. 2. Time series of the LC position defined by the northernmost location of the LC axis based on the satellite altimetry data (blue line) and the HYCOM reanalysis (red line). The green dots indicate the dates of extended phase, with the dark green ones marking the dates of retracted phase.

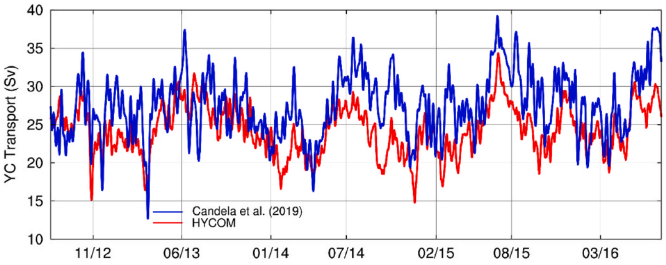

Fig. 3. Time series of the transport through the YC estimated from mooring records (red; the same as Fig. 5 in Candela et al., 2019) and HYCOM (blue). Both time series have been low-pass filtered to elimate signals with periods shorter than 7 days. The correlation between the two time series is 0.65, significant at the 99% confidence level.

2.2. *Information-flow based causality analysis*

Causal inference is a subject of wide interest in most scientific disciplines. In oceanography, a common practice is conducting correlation and/or regression analyses to quantify the relationship between one time series and another. However, it is known that correlation does not necessarily imply causality. Another widely used practice is performing a statistical hypothesis test (Granger, 1969) based on the usefulness of one time series for predicting another. This kind of approach has been found to induce spurious causality under many conditions (e.g., Stokes and Purdon, 2017). On the other hand, another notion, namely, information flow (or information transfer), or IF for short, has been studied in physics for decades (e.g., Vastano and Swinney, 1988; Schreiber, 2000; Liang and Kleeman, 2005), which has been gradually recognized to be connected with causality (see Liang, 2016 for a review). However, due to the axiomatic formulation, this connection has been frequently questioned (e.g., Lizier and Prokopenko, 2010; Smirnov, 2013). It had not been rigorously formulated until recently when causality comes as a natural corollary (Liang, 2016). For practical purpose, its maximum likelihood estimator with respect to time series has been obtained, which results in rather concise, easy-to-use formulas (Liang, 2008, 2014, 2016, 2018, 2021). In the following, we give a brief description of this formalism within the framework of differentiable fields (hence applicable to ocean problems) for two variables. A complete derivation is referred to Liang (Liang, 2008, 2014, 2016, 2021) and references therein.

Given a two-dimensional (2D) dynamical system with stochasticity included,

$$\frac{d\mathbf{X}}{dt} = \mathbf{F}(\mathbf{X}, t) + \mathbf{B}(\mathbf{X}, t)\dot{\mathbf{W}}, \tag{1}$$

where $\mathbf{X} = (X_1, X_2)$ are the state variables of the 2D system, $\mathbf{F} = (F_1, F_2)$ is the vector of drift coefficients which can be arbitrary nonlinear functions of $\mathbf{X}$ and t, , $\mathbf{B} = (b_{ij})$ is a matrix of diffusion coefficients (stochastic perturbation amplitudes) which may also be functions of $\mathbf{X}$ and t, and $\dot{\mathbf{W}} = (\dot{W}_1, \dot{W}_2)$ is the white noise vector ($\mathbf{W}$ is a standard 2D Wiener process). If a deterministic system, say the ocean system, then simply let the matrix of stochastic perturbation $\mathbf{B} = \mathbf{0}$. As the system evolves from one state to another, its entropy (uncertainty) changes accordingly. The IF from one component, say X_2, to another, say X_1, written $T_{2\rightarrow1}$, is the contribution of X_2 to the time rate of change of the marginal entropy of X_1. The derivation is rather technically involved.

Interested readers are referred to Liang (2008). Nevertheless, the final result is quite concise, which is

$$T_{2\to1} = -E\left[\frac{1}{\rho_1}\frac{\partial(F_1\rho_1)}{\partial x_1}\right] + \frac{1}{2}E\left[\frac{1}{\rho_1}\frac{\partial^2\left(b_{11}^2+b_{12}^2\right)\rho_1}{\partial x_1^2}\right], \tag{2}$$

where ρ_1 is the marginal probability density of X_1, and E signifies mathematical expectation. For deterministic dynamical systems, only the first term on the right-hand side of Eqn. (2) retains. The unit of IF is nats per unit time (nat is natural unit of information). The resulting IF is asymmetric between X_1 and X_2, i.e. $T_{2\to1} \neq T_{1\to2}$, quite different from the correlation analysis that is symmetric in nature. More importantly, it satisfies the principle of nil causality (proof is referred to Liang 2016), that is, if the evolution of X_1 is independent on X_2, then $T_{2\to1} = 0$. Otherwise, $T_{2\to1} \neq 0$. In contrast, many traditional formalisms have been reported to fail to verify this principle in many situations, while here it appears as a proven theorem. Different from other statistical methods that only provide a yes-or-no judgment, the IF-based formalism allows for an inference of both the direction and magnitude of the causality between variables.

The strength of the causality is measured by the magnitude (absolute value) of IF. Note that here a nonzero $T_{2\to1}$ can be either positive or negative; a positive (negative) $T_{2\to1}$ means that X_2 contributes to the increase (decrease) of the marginal entropy of X_1 (Liang, 2014). Since the present study focuses on the causal relation between the LC penetration and inflow/outflow conditions, we only need to consider the magnitude of IF.

The above formula has been validated in many highly chaotic systems, such as baker transformation, Hénon map, Langevin equation, etc. (Liang, 2014, 2016), and has just been generalized to the quantum domain involving quantum entanglement (Yi and Bose, 2022). In the case when only two time series are available, Liang (2014) showed that the IF can be statistically estimated. In the linear limit, the maximum likelihood estimator of the IF from X_2 to X_1 proves to be

$$\widehat{T}_{2\to1} = \frac{C_{11}C_{12}C_{2,d1} - C_{12}^2C_{1,d1}}{C_{11}^2C_{22} - C_{11}C_{12}^2}, \tag{3}$$

where C_{ij} is the sample covariance between X_i and X_j $(i, j = 1, 2)$, $C_{i,dj}$ is the covariance between X_i and $\dot{X}_j$, and $\dot{X}_j$ denotes the difference approximation of dX_j/dt using the Euler forward scheme. Although under a linear assumption, Eqn. (3) has been validated in highly nonlinear system problems (Liang, 2014), and has been applied with success to many realistic problems in atmosphere-ocean science, data science, financial economics and neuroscience (e.g., Stips et al., 2016; Hristopulos et al., 2019; Lu et al., 2022; Liang et al., 2021), to name a few. Note that Eqn. (3) gives the instantaneous causality, while the delayed causality can be inferred using delayed time series which has been exercised in making causal AI-based climate predictions (see, for example, Liang et al., 2021). All results presented in this study are instantaneous causalities as the magnitudes of the measured causalities generally decrease with increasing lags (not shown).

To quantify the relative importance of causalities among various factors, the above formula need be further normalized. As established in Liang (2008), the time rate of change of the marginal entropy of X_1, written $\frac{dH_1}{dt}$, consists of three components:

$$\frac{dH_1}{dt} = \frac{dH_1^*}{dt} + \frac{dH_1^{\text{noise}}}{dt} + T_{2\to1}, \tag{4}$$

where the first (second) term on the right-hand side stands for the time rate of change of H_1 due to X_1 itself without (with) stochasticity, and the third term is the very IF from X_2 to X_1. The derivation of $\frac{dH_1^*}{dt}$ and $\frac{dH_1^{\text{noise}}}{dt}$ can be found in Liang (2008). Using $\left|\frac{dH_1^*}{dt}\right| + \left|\frac{dH_1^{\text{noise}}}{dt}\right| + |T_{2\to1}|$ as the normalizer, Liang (2015) obtained the normalized form of Eqn. (2) as

$$\tau_{2\to1} = \frac{T_{2\to1}}{\left|\frac{dH_1^*}{dt}\right| + \left|\frac{dH_1^{\text{noise}}}{dt}\right| + |T_{2\to1}|}. \tag{5}$$

If $\tau_{2\to1} = 1$, the evolution of H_1 is totally due to the IF from X_2; if $\tau_{2\to1} = 0$, then X_2 is not causal to X_1. Therefore, $\tau_{2\to1}$ can be used to quantify the importance of X_2 to X_1 relative to other processes. The maximum likelihood estimator of $\tau_{2\to1}$ can be obtained following the same procedure (Liang, 2015). All IFs shown in the result section of the present paper have been normalized and are termed as relative IF and denoted as τ. (We purposely drop the hat to avoid notational complexity.)

Finally, statistical significance test is needed to see whether the estimated IF is statistically significant. Liang (2014) introduced the Fisher information matrix $\mathbf{I} = (I_{ij})$

$$I_{ij} = -\frac{1}{N}\sum_{n=1}^{N}\frac{\partial^2 \log \rho(\mathbf{X}_{n+1}|\mathbf{X}_n;\widehat{\theta})}{\partial\theta_i\partial\theta_j}, \tag{6}$$

where N is the data points, $\widehat{\theta}$ is the vector of IF-related parameters to be estimated, and $\rho(\mathbf{X}_{n+1}|\mathbf{X}_n)$ is a Gaussian for a linear model. Given a level, the significance of an estimated IF can be tested. In this study, all given confidence intervals are at the 99% level.

3. Results

3.1. *Dominant transport and vorticity flux mode in the entry and exit channels and their relationship with LC penetration*

We first perform a singular value decomposition (SVD) analysis to identify dominant pairs of modes of the LC variation and flow conditions (i.e. transport and vorticity flux) in the entry and exit channels. Fig. 4a and b displays the spatial patterns of the first SVD mode (containing 86% of the total covariance) between the SSH in the GoM and the along-channel velocity in the YC. Their corresponding temporal coefficients [denoted as $\eta^{\text{SVD}}(t)$ and $V_{\text{YC}}^{\text{SVD}}(t)$] are shown in Fig. 4d and e. The simultaneous correlation between the two series is 0.56 (statistically significant over the 99% confidence level), indicating a close linkage between the SSH and inflow velocity variability. The SSH SVD pattern is similar to the pattern revealed by the leading Empirical Orthogonal Function (EOF) in previous studies (e.g., Liu et al., 2016). Its associated temporal coefficient (η^{SVD}) is highly correlated with the LC latitudinal position with no appreciable lag (Fig. 4d), indicating that η^{SVD} can be used as an index of the LC path fluctuation. Here we choose η^{SVD} rather than the LC position as the LC path index because the latter has discontinuities at times when an eddy is shed, which may produce spurious result using Eqn. (3) Also note that the LC path index represents not only the growth and wane of the LC but also the detachment events (see the discontinuities in Fig. 2; these events seem to occur more frequently in the HYCOM reanalysis than the observation). Several short-period detachments and reattachments (generally last several days to weeks) could occur before an LC eddy is fully shed. These short-period events, which are not the focus of the present study, seem even more chaotic than the lower-frequency growth and wane of the LC. Previous studies have reported that the short-period detachments are caused by the movement of frontal cyclonic eddies (especially in the east side of the LC) that are generated by the instability of the penetrated LC (Donohue et al., 2016; Rudnick et al., 2014; Smith et al., 2014; Yang et al., 2020). In other words, they are more likely to be intrinsically generated.

The dipole seesaw-like pattern of the along-channel velocity in the YC (Fig. 4b) indicates that the expansion of the LC is associated with an increase of transport on the western channel and a reduction in the central and eastern channel. The net transport through the YC ($V_{\text{YC}}^{\text{Int}}$) is decreasing when the LC extends, indicated by the negative correlation between η^{SVD} and $V_{\text{YC}}^{\text{Int}}$ (Fig. 5a and 6a), consistent with previous studies

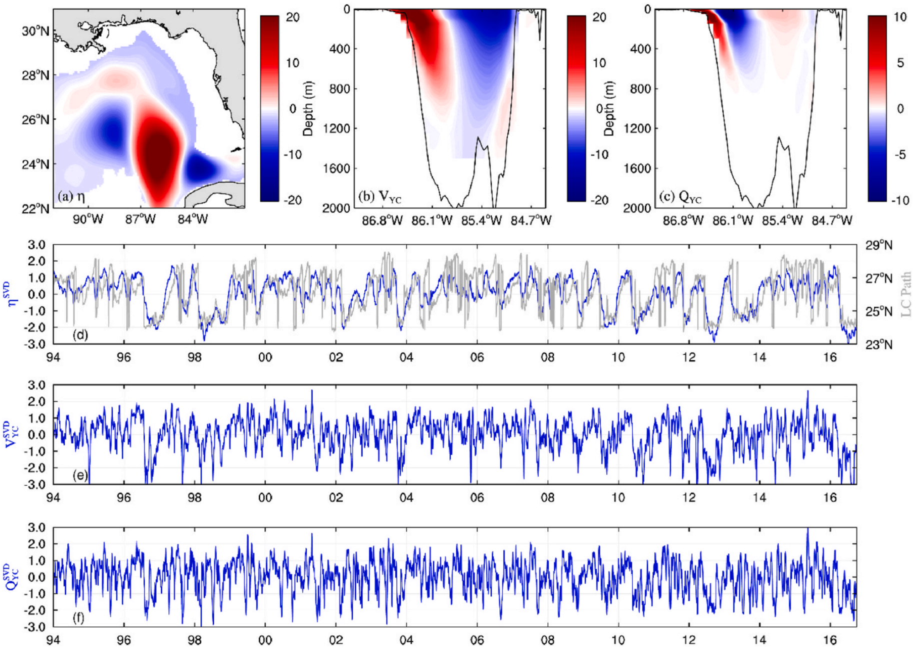

Fig. 4. The leading SVD mode between the SSH (η) over the eastern GoM and the along-channel velocity (V_{YC})/vorticity flux (Q_{YC}) in the Yucatan Channel. (a)–(c) Spatial patterns for η, V_{YC} and Q_{YC}, respectively. The maps are obtained by regressing the data onto their respective standardized temporal coefficients, so that the amplitude of each map has the same unit as their original data. Positive value indicates flow into the GoM. The SSH data in coastal regions with depth shallower than 100 m is removed before the SVD analysis. (d)–(f) Standardized temporal coefficients for η, V_{YC} and Q_{YC} (denoted as η^{SVD}, $V_{\mathrm{YC}}^{\mathrm{SVD}}$ and $Q_{\mathrm{YC}}^{\mathrm{SVD}}$, respectively; blue lines). Note here only the pattern and coefficient of η for the SVD analysis between η and V_{YC} is shown. Those of η for the SVD analysis between η and Q_{YC} is not shown as they are almost identical to Fig. 4a and d. The superimposed grey line in (d) is the time series of LC position.

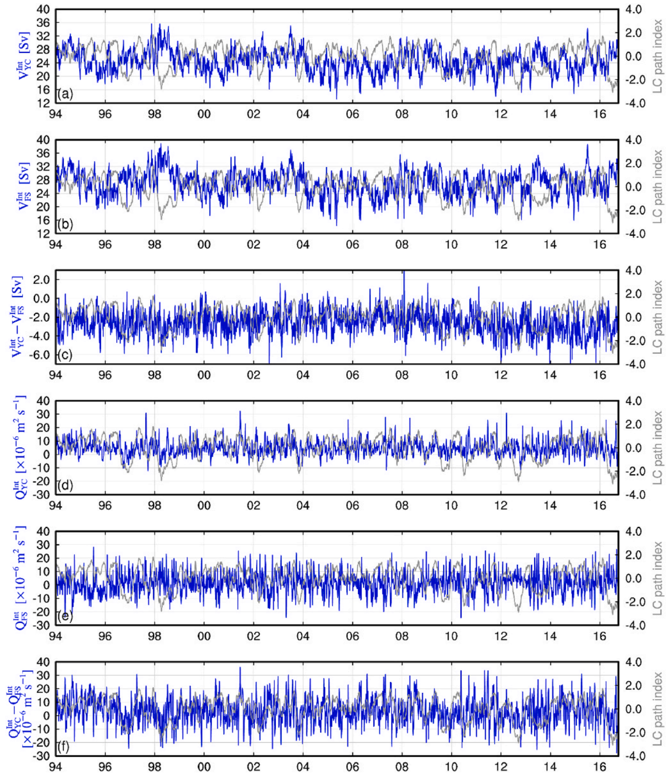

Fig. 5. Time series of transport (in Sv) and vorticity flux (in 10^{-6} m^2 s^{-1}) in the two channels. (a) Net transport through the YC ($V_{\mathrm{YC}}^{\mathrm{Int}}$); (b) net transport through the FS ($V_{\mathrm{FS}}^{\mathrm{Int}}$); (c) net transport through the GoM ($V_{\mathrm{YC}}^{\mathrm{Int}} - V_{\mathrm{FS}}^{\mathrm{Int}}$). (b–e) As in (a–c), but for the vorticity flux. The LC path index (η^{SVD}) is superposed in each figure with grey line.

(e.g., Sheinbaum et al., 2002; Lin et al., 2009). The lead-lag correlation reveals that the minimum $V_{\mathrm{YC}}^{\mathrm{Int}}$ tends to occur about two weeks after the maximum η^{SVD} (red line in Fig. 6a), which is at odds with the almost simultaneous correlation between η^{SVD} and $V_{\mathrm{YC}}^{\mathrm{SVD}}$ (blue line in Fig. 6a). This suggests that $V_{\mathrm{YC}}^{\mathrm{Int}}$ and $V_{\mathrm{YC}}^{\mathrm{SVD}}$ are different proxies for the transport variation in the YC. The former is the net transport through the channel, while the latter mainly represents the cross-channel spatial pattern of the transport variability (transport at the other side have an almost inverse anomaly; Fig. 4b). In the next subsection, both proxies will be used to identify their casual links with the LC extension.

Fig. 4c and f shows the leading SVD mode between the SSH and vorticity flux though the YC. The spatial pattern and temporal coefficient of the SSH field are not shown as they are almost identical to Fig. 4a and d. The correlation between the coefficient series (η^{SVD} and $Q_{\mathrm{YC}}^{\mathrm{SVD}}$) of this mode ($r = 0.42$) is slightly lower than that between η^{SVD} and $V_{\mathrm{YC}}^{\mathrm{SVD}}$. This mode exhibits a tripole structure in the YC (Fig. 4c) which indicates that the expansion of the LC is associated with a strong positive-negative alternating vorticity influx concentrated on the western slope of the YC and a weak positive influx on the eastern channel. The two cores in the west have much higher amplitude than the eastern one. The area integral across the section (i.e. $Q_{\mathrm{YC}}^{\mathrm{Int}}$) is very different from $Q_{\mathrm{YC}}^{\mathrm{SVD}}$ (compare Fig. 4f and 5d), and the correlation between $Q_{\mathrm{YC}}^{\mathrm{Int}}$ and η^{SVD} is quite low (red line in Fig. 6b), contrasting with the significant correlation between $Q_{\mathrm{YC}}^{\mathrm{SVD}}$ and η^{SVD} (blue line in Fig. 6b).

With regard to the coupling between flow variability in the FS and the LC, we find that the expansion of the LC is associated with an increased transport on the northern side of the strait and a decreased transport to the south (Fig. 7b). The net transport through the FS ($V_{\mathrm{FS}}^{\mathrm{Int}}$) is anticorrelated with η^{SVD} with a lag of about two weeks (Fig. 5b and 6c), consistent with previous studies (Hirschi et al., 2019; Lin et al., 2010). The SVD pattern of the vorticity outflux through the FS is characterized by a negative core in the center of the strait and positive core to the north as well as the south (Fig. 7c). This mode seems less correlated with the LC path variation ($r = 0.18$; not statistically significant over the 99% confidence level). The correlation between the integral vorticity outflux ($Q_{\mathrm{FS}}^{\mathrm{Int}}$) and η^{SVD} is also quite low, with $r = 0.22$ (statistically significant over the 99% confidence level) when η^{SVD} leads $Q_{\mathrm{FS}}^{\mathrm{Int}}$ by about 11 days (Fig. 6d).

Besides the above-described relations, it is also worth exploring the correlations of flow variability between the two channels. As shown in Fig. 6e, the $V_{\mathrm{YC}}^{\mathrm{Int}}$ is highly correlated with $V_{\mathrm{FS}}^{\mathrm{Int}}$ with no lag, consistent with the observation (Candela et al., 2019), while $V_{\mathrm{YC}}^{\mathrm{SVD}}$ does not show a significant correlation with the $V_{\mathrm{FS}}^{\mathrm{SVD}}$. The correlation differences between the integral and SVD time series imply that they are different

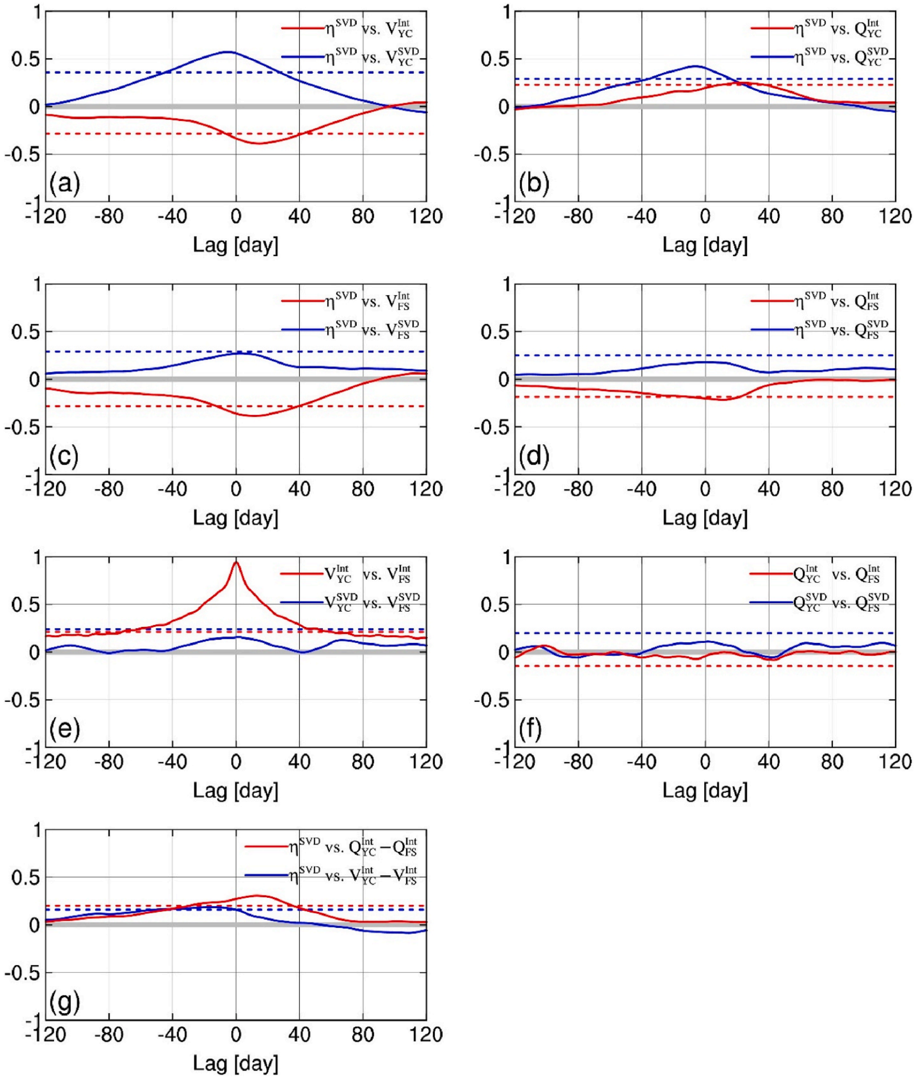

Fig. 6. Lead-lag correlations between various time series. A positive lag means that the first time series leads the latter. The dashed line in each figure indicates the 99% confidence level for the corresponding correlation coefficient with the same color.

proxies for the velocity variation in the channels. The vorticity flux proxies in the two channels are not well correlated for either the SVD coefficients or integral series (Fig. 6f). We also test Maul (1977)'s idea and find weak correlation between the net transport through the GoM (i.e. $V_{\mathrm{YC}}^{\mathrm{Int}} - V_{\mathrm{FS}}^{\mathrm{Int}}$) and the LC path variation (Fig. 6g). The net vorticity flux through the GoM (i.e. $Q_{\mathrm{YC}}^{\mathrm{Int}} - Q_{\mathrm{FS}}^{\mathrm{Int}}$) is positively correlated with η^{SVD}, although with a weak correlation of 0.19 (statistically significant over the 99% confidence level) when the η^{SVD} leads by about two weeks (Fig. 6g).

The above analysis based on long time series of the HYCOM reanalysis describes the correlations of the LC path and the transport and vorticity flux in the YC and the FS. It should be noted that the correlations do not necessarily imply causality. In the following subsections, we will use the IF- and data-based causal inference method to investigate these complex relations, which otherwise would be difficult, if not impossible, to investigate.

It is also worth mentioning that the SVD coefficient series (i.e. $V_{\mathrm{YC}}^{\mathrm{SVD}}$, $V_{\mathrm{FS}}^{\mathrm{SVD}}$, $Q_{\mathrm{YC}}^{\mathrm{SVD}}$ and $Q_{\mathrm{FS}}^{\mathrm{SVD}}$) and integral series (i.e. $V_{\mathrm{YC}}^{\mathrm{Int}}$, $V_{\mathrm{FS}}^{\mathrm{Int}}$, $Q_{\mathrm{YC}}^{\mathrm{Int}}$ and $Q_{\mathrm{FS}}^{\mathrm{Int}}$) reflect distinct perspectives of the flow variability in the two channels. Unlike the integral series that only represents the net flux of volume/vorticity through the section, the SVD series contains more local information of the variable (note that there is strong compensation of out-of-phase anomalies across the channel). Using 59-months direct mooring measurements, Athié et al. (2019) raised caution about the difference between the transport through the YC and that through only the western YC (west of 85.6°W). They noticed that the two transport indices are very different since the transports through the western and eastern channel are overall out of phase, similar to the one found in this study. Their correlation analysis also shows that the western-channel transport index (analogous to $V_{\mathrm{YC}}^{\mathrm{SVD}}$ in this study) is more related with the LC extension. In the following, both the SVD coefficient series and the integral series will be used as indices for the flow conditions at the entry and exit channels. One may argue that the SVD coefficient series used in this study only reflects the dominant mode that is linked to the LC behavior thanks to the property of SVD analysis, rather than the dominant mode of the variable itself. In view of this issue, we have performed additional EOF analysis on the velocity and vorticity flux in the two channels and found that the spatial patterns as well as temporal coefficients of the leading EOF mode are almost the same as those obtained from the SVD analysis (not shown). This confirms that the dominant component of the inflow/outflow transport/vorticity flux variability is indeed dynamically connected to the LC extension.

3.2. *Causal relationship revealed by the IF-based formalism*

In the previous subsection, we have carried out SVD and correlation

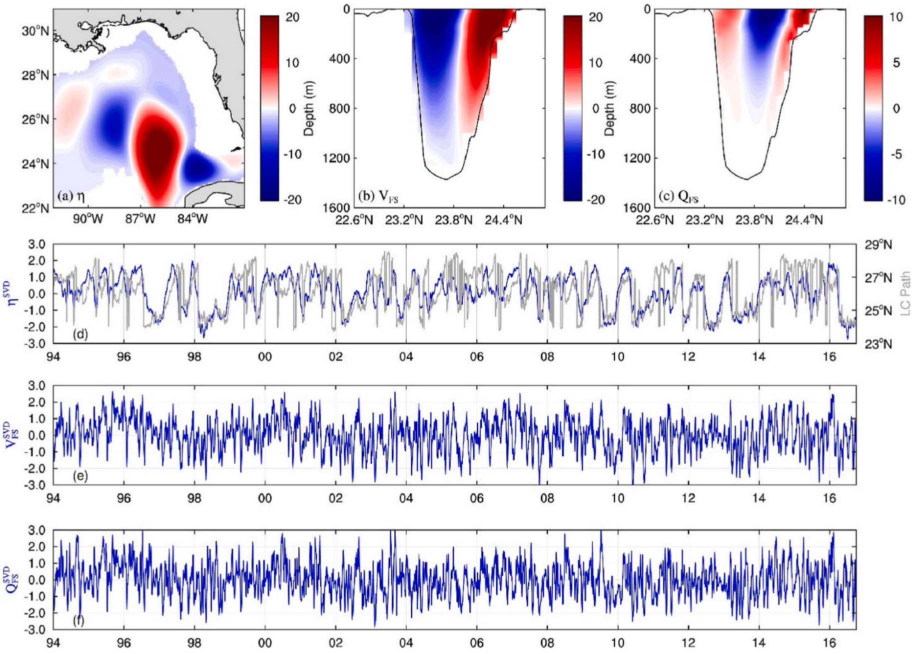

Fig. 7. As in Fig. 4, but for the along-channel velocity (V_{FS})/vorticity flux (Q_{FS}) in the Straits of Florida.

analyses and established the connectivity between the LC extension and transport/vorticity flux in the two channels. These correlations, high or low, however, do not provide a "who drives who" judgment. In the following, we will approach the problem by using the IF-based causal inference tool. Also shown are their associated spatial structures, thanks to the quantitative nature of the formalism.

Table 1 summarizes the rates of relative IFs between various indices introduced in the previous subsection. A noticeable feature of the IFs between the LC path (indicated as η^{SVD}) and inflow variables (i.e. $V_{\mathrm{YC}}^{\mathrm{SVD}}$, $Q_{\mathrm{YC}}^{\mathrm{SVD}}$, $V_{\mathrm{YC}}^{\mathrm{Int}}$ and $Q_{\mathrm{YC}}^{\mathrm{Int}}$) is that the causalities are asymmetric, that is, the one from the latter to the former are much larger than the reverse. The only significant IF from η^{SVD} to the four YC-related variables is the one to $V_{\mathrm{YC}}^{\mathrm{Int}}$ ($|\tau| = 10.7\%$), though with a smaller value compared to the reverse flow ($|\tau| = 48.43\%$). The almost one-way causality suggests that transport and vorticity flux in the YC cause the LC extension, while the LC path state is less causal to the current variability in the YC.

In contrast to the YC, the IFs from the FS-related variables to the LC index is generally small (though significant), suggesting that the flow structures in the FS have less impact on the LC extension than those in the YC. An exception is that the total transport through the FS ($V_{\mathrm{FS}}^{\mathrm{Int}}$) has a strong influence on the LC ($|\tau| = 47.88\%$). Additionally, a one-way causality is identified from the $V_{\mathrm{YC}}^{\mathrm{Int}}$ to $V_{\mathrm{FS}}^{\mathrm{Int}}$ ($|\tau| = 35.55\%$), as well as from the net transport through the GoM ($V_{\mathrm{YC}}^{\mathrm{Int}} - V_{\mathrm{FS}}^{\mathrm{Int}}$) to η^{SVD} ($|\tau| = 19.45\%$). These results indicate that the YC transport is causal to the LC extension as well as the FS transport, and the FS transport and the net transport through the GoM are also causal to the LC extension. Similar conclusion can be obtained by looking at the net vorticity flux through the two channels.

Table 1
Relative IFs (in absolute value; unit: %) between various variables. Values significant at the 99% level and with an absolute value larger than 10% are shown in bold.

X_1	X_2	$\lvert\tau_{X_1\to X_2}\rvert$ ($\lvert\tau_{X_2\to X_1}\rvert$)
η^{SVD}	$V_{\mathrm{YC}}^{\mathrm{SVD}}$	2.34 (**39.79**)
η^{SVD}	$Q_{\mathrm{YC}}^{\mathrm{SVD}}$	0.92 (**36.63**)
η^{SVD}	$V_{\mathrm{YC}}^{\mathrm{Int}}$	**10.70** (**48.43**)
η^{SVD}	$Q_{\mathrm{YC}}^{\mathrm{Int}}$	3.38 (**43.11**)
η^{SVD}	$V_{\mathrm{FS}}^{\mathrm{SVD}}$	4.44 (**17.64**)
η^{SVD}	$Q_{\mathrm{FS}}^{\mathrm{SVD}}$	1.57 (0.22)
η^{SVD}	$V_{\mathrm{FS}}^{\mathrm{Int}}$	**10.32** (**47.88**)
η^{SVD}	$Q_{\mathrm{FS}}^{\mathrm{Int}}$	2.38 (**14.10**)
η^{SVD}	$V_{\mathrm{YC}}^{\mathrm{Int}} - V_{\mathrm{FS}}^{\mathrm{Int}}$	0.73 (**19.45**)
η^{SVD}	$Q_{\mathrm{YC}}^{\mathrm{Int}} - Q_{\mathrm{FS}}^{\mathrm{Int}}$	5.03 (**46.13**)
$V_{\mathrm{YC}}^{\mathrm{SVD}}$	$V_{\mathrm{FS}}^{\mathrm{SVD}}$	1.98 (0.74)
$V_{\mathrm{YC}}^{\mathrm{Int}}$	$V_{\mathrm{FS}}^{\mathrm{Int}}$	**35.55** (0.32)
$Q_{\mathrm{YC}}^{\mathrm{SVD}}$	$Q_{\mathrm{FS}}^{\mathrm{SVD}}$	0.95 (0.10)
$Q_{\mathrm{YC}}^{\mathrm{Int}}$	$Q_{\mathrm{FS}}^{\mathrm{Int}}$	0.24 (0.62)

We further examine the spatial patterns of causality, or causal structures, over the GoM by performing the same analysis to the gridded SSH field. Fig. 8 displays the causality maps from the 10 indices extracted at the two channels to the SSH. The causal structures from $V_{\mathrm{YC}}^{\mathrm{SVD}}$ and $Q_{\mathrm{YC}}^{\mathrm{SVD}}$ are similar, both of which are maximized along the western branch of the LC as well as its extension area (Fig. 8a and b). The IF from the total YC transport ($V_{\mathrm{YC}}^{\mathrm{Int}}$) also shows large values in the LC area with a maximum center around 85°W, 25°N (Fig. 8c). Another center appears near the southwestern corner of the West Florida Shelf where strong interaction between the LC and the shelf occurs (Weisberg and Liu, 2017). The above results demonstrate that the transport and vorticity flux in the YC indeed have a strong impact on the SSH variability in the LC area. Interestingly, from the feature-rich causality maps, one can see that the flow variability in the YC also exerts influence on their upstream current (see the strong IF in the northwestern Cayman Basin in Fig. 8a, b and 8d). The maximum center around 85°W, 19°N is collocated with the time-mean anticyclonic recirculation south of the YC. The mechanism for this downstream-to-upstream merits further investigation in future work. It is possible that the inflow could be blocked or allowed by the presence of mesoscale eddies passing through the YC, which could impact the upstream flow in the Caribbean Sea. In addition, there are also some small but significant causalities at some locations in the Caribbean Sea (Fig. 8c and g), implying that a small part of the SSH variability at these locations is influenced by the flow variability in the two channels, although the mechanism is not clear at present. Nevertheless, the IFs in these remote locations are much smaller in magnitude (generally <10%) than the ones found near the LC region, suggesting that the inflow/outflow variabilities mainly influence the SSH variability in the vicinity of the LC.

Fig. 8e–h shows the IF patterns from the FS indices (i.e. $V_{\mathrm{FS}}^{\mathrm{SVD}}$, $V_{\mathrm{FS}}^{\mathrm{Int}}$,

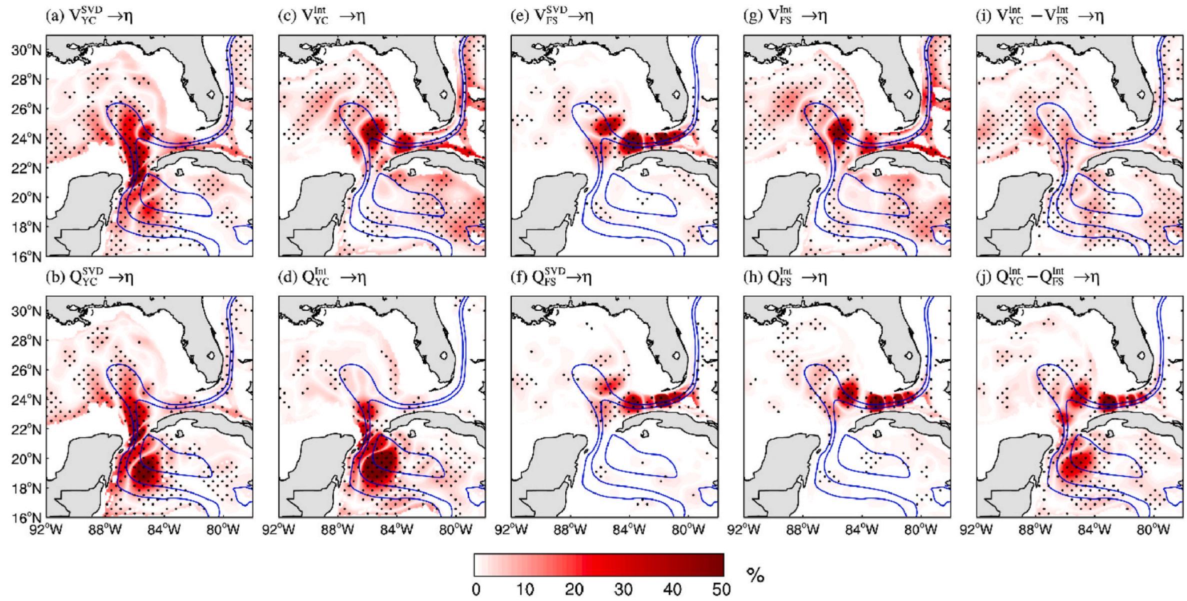

Fig. 8. Spatial patterns of the IFs from various time series derived in the YC and the FS to the gridded SSH field from the HYCOM reanalysis. Strippled are regions where the IFs are significant at the 99% confidence level. Blue contours denote the 0.17-, 0.3- and 0.47-m time-mean SSH isolines.

Q_{FS}^{SVD} and Q_{FS}^{Int}) to the SSH. The four maps all display weak causality in the western branch of the LC but a strong train of causality along the eastern branch of the LC (from around 85°W, 24°N to the exit). This suggests that the current variability in the FS mainly influences the eastern branch of the LC. Using observed transport cable data, Sturges et al. (2010) found pulses of increased Florida Current transport prior to LC eddy shedding. They conjectured that these downstream pulses may trigger instability which finally leads to eddy shedding. To the best of our knowledge, Sturges et al. (2010) is the only study considering the FS current variability as a cause rather than a consequence of the LC as proposed in many previous studies (e.g., Lin et al., 2010; Mildner et al., 2013; Hirschi et al., 2019). The significant IFs from the FS indices to the LC, though smaller than that from the YC counterpart, seems to support Sturges et al. (2010)'s idea. The exact dynamics underlying such downstream influence path remains unclear yet and this warrants further study with more observations in the exit flow region (Zhang et al., 2019; e.g., Liu et al., 2021).

Interestingly, our results also show a significant IF from the transport through the two channels (i.e. V_{YC}^{Int}; V_{FS}^{Int}) to the Gulf Stream along the southeastern U.S. continental shelf. Recently, Hirschi et al. (2019) proposed a volume continuity argument that the modulation of the LC length (due to the expansion and retraction of the LC) determines the transport out of the GoM and hence that of the Gulf Stream. Combining Hirschi et al. (2019)'s result and ours, we can infer that the flow conditions in the YC and the FS (primarily the former) causes the LC extension, which further exerts influence on the transport through the FS and the further downstream Gulf Stream. The net volume transport through the GoM exhibits weak (but still statistically significant) impact on the SSH variability in the LC area (Fig. 8i). In contrast, the IF of the SSH field from the net vorticity flux exhibits a train of causal centers

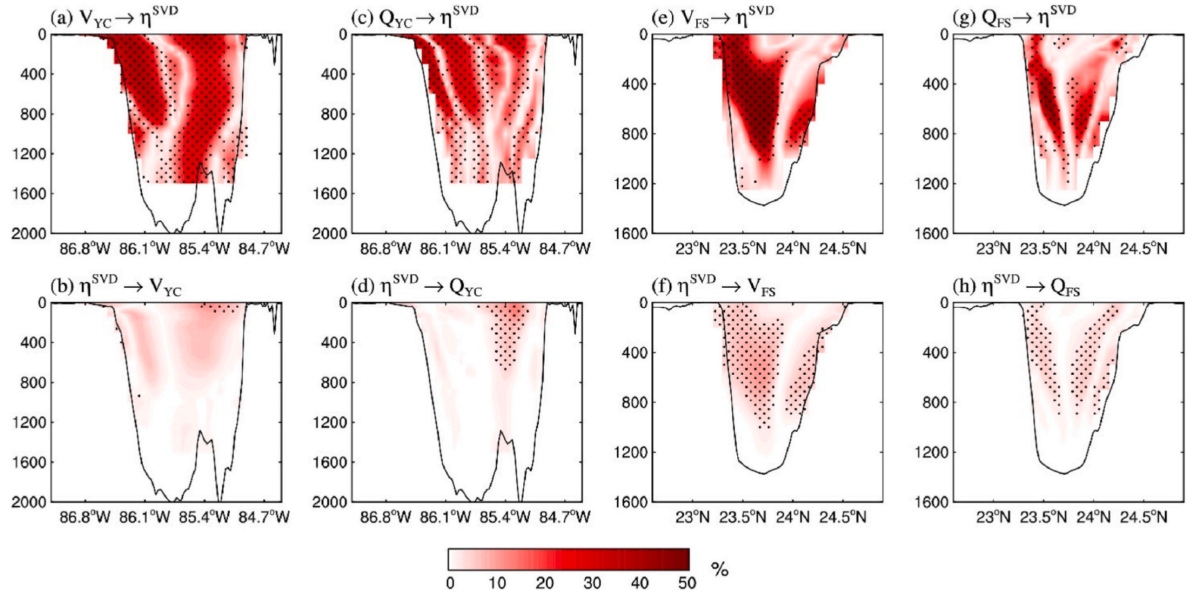

Fig. 9. Spatial patterns of the IFs between the along-channel velocity/vorticity flux and the LC path index (η^{SVD}) in (a)–(d) the YC and (e)–(h) the FS based on the HYCOM analysis. Strippled are regions where the IFs are significant at the 99% confidence level.

from the entry to the exit portal, generally following the 0.3-m time-mean SSH isoline. This indicates that the net vorticity flux through the GoM may be more important in determining the LC extension than the net transport. Further analysis using a vorticity budget may be helpful in understanding the underlying dynamics of the LC modulation.

Fig. 9 displays the vertical structures of IFs between the LC path index (η^{SVD}) and along-channel velocity and vorticity flux in the YC and FS. These figures show an asymmetry of causality, that is, the causality from the velocity (vorticity flux) at the two channels to the LC path variation is much larger in magnitude than that in the reverse direction. More importantly, the causality has its own structures. For example, the IF from the YC velocity to the LC has large values in the western and eastern sides of the channel with the western center stronger but the eastern one more deep-reaching (Fig. 9a), corresponding to the seesaw-like SVD pattern shown in Fig. 4b. The inverse IF is weak and almost insignificant throughout the channel. The causal structure from the YC vorticity flux is more complex, with four maximum bands distributed across the channel (Fig. 9c). Interestingly, a weak but significant area around 85.4W and above 800-m depth is identified in the inverse IF section (Fig. 9d), which coincides with the positive center in the SVD pattern in Fig. 4c. This suggests that the LC can also drive the vorticity flux in the YC, but its influence is limited in a small area in the eastern channel with a vertical extent of 800 m. In contrast to the YC case, the LC path index and the flow velocity (vorticity flux) in the FS are mutually causal, although the IF from the former to the latter is much smaller than the reserve (Fig. 9e–h). High causality centers are found in the southern and northern straits, with a weak center in between.

3.3. *Results from a free running multidecadal simulation*

In the previous subsection, we have quantified the causal links between the flow conditions in the two channels and the LC extension based on the data-assimilative HYCOM reanalysis, which is considered as a realization of the real ocean due to its faithful skill in reproducing the observed features (see the quantitative assessment in section 2.1). Even though the HYCOM reanalysis output is close to the observation, one may argue that the data assimilation procedure will break the balance of the model equations and therefore may lead to spurious relations between physical processes. To see whether the causal relations obtained in section 3.2 are robust or not, we additionally perform the same analysis to the outputs from a free running 54-yr simulation. Since the free running model is repeatedly forced by the same realistic atmospheric forcing, it provides us three realizations with different initial conditions. With this unique dataset, we are able to discover whether the intrinsic (or chaotic) variability within the LC system would change the causal influence imposed by the forcings at the inflow/outflow portals as identified in the previous subsection.

Though driven by identical forcings, the LC path variations in the three simulation cycles are substantially different (Fig. 10). During most of the time, the LC path modulations in the three realizations share no common phase. This indicates that intrinsic variability generated by nonlinearities is important in the LC dynamics, in agreement with the results of Garcia Gomez (2020) who suggested that intrinsic variability dominates the sea level anomaly variability in the LC region using a 50-member ensemble simulations. Figs. 11 and 12 illustrate the similarity and difference of the causal patterns among the three simulation cycles. Interestingly, though with very different LC path phases, the IFs from the flow variability in the two channels to the LC are quite similar. This implies that the intrinsic variability does not significantly change the causality imposed by the inflow/outflow forcings. More importantly, the casual relations in the free running simulation are generally in agreement with the those obtained from the reanalysis. There are large IFs from the transport and vorticity flux in the YC to the SSH occupying in the LC and its extension area, while those associated with the FS are mostly confined to the eastern branch of the LC (compare Fig. 11 with Fig. 8). Apart from the similarities, there are also noticeable differences between the two datasets. For example, the strength of IFs in the free run simulation is generally larger than those in the reanalysis. From the vertical sections (Fig. 12), one can more clearly identify the differences. The LC's influence on the YC transport and vorticity flux is quite strong in the free run simulation (Fig. 12b and d), contrasting with the weak influence identified in the reanalysis (Fig. 9b and d). The causal link from the LC to the FS current variability is very weak in the free run simulation (Fig. 12f and d), in contrast with the significant causality in the reanalysis. In addition, we find substantial differences of the causal strength among the three cycles of simulations. For example, the FS transport has higher influence on the LC path in the second cycle of the simulation than those in the other two cycles. This indicates that the strength of the causal links between these variables could vary among different realizations of simulations due to intrinsic nonlinearity of the model. There is no doubt that much more ensemble members are needed to assess the ensemble spread of the causal influence imposed by the inflow/outflow forcings as reported in this study. Nevertheless, the robust asymmetric causality appearing in all three simulation cycles adds more credibility to the causal relations revealed in the reanalysis.

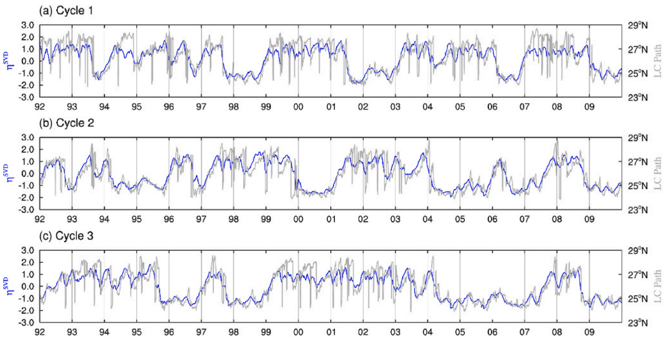

Fig. 10. Time series of the SVD coefficient for η (blue line) and LC position (grey line) based on the free-running HYCOM 54-year experiment. The three cycles are produced by the same 18-year record of surface forcing (repeated three times).

4. Conclusion and discussion

The relation between the inflow/outflow conditions and the penetration of LC into the GoM has been considered as one of the most critical gaps that prevents physical oceanographers from understanding and predicting the LC system (National Academies of Sciences, E., 2018). In this study, the recently developed information flow (IF)-based causal inference method, which is quantitative in nature, data-driven by design and is rigorously developed from first principles in physics, is applied for the first time to address the problem.

We first use a 23-year (1994–2016) HYCOM reanalysis product to revisit the correlations between the LC extension and transport/vorticity flux in the Yucatan Channel (YC) and Straits of Florida (FS). The long-term time series allows us to identify statistically significant correlations, if any, between the two parties. It is found that when the LC is more extended, the transport on the western (northern) side of the YC (FS) increases, and that on the eastern (southern) side of the YC (FS) decreases. Meanwhile, both net transports through the two channels decrease. Regarding the vorticity flux in the two channels, the LC's extension is associated with a narrow strip of positive vorticity flux along the western (northern) YC (FS) slope and negative vorticity flux to its east (south), and again positive in the eastern (southern) channel. These relationships, though significant from a perspective of correlation, do not necessarily imply causality.

By applying the IF-based causal inference method, we distinguish the causalities from the variable correlations embedded within the complex system. Particularly, a clear asymmetry of causality between the flow

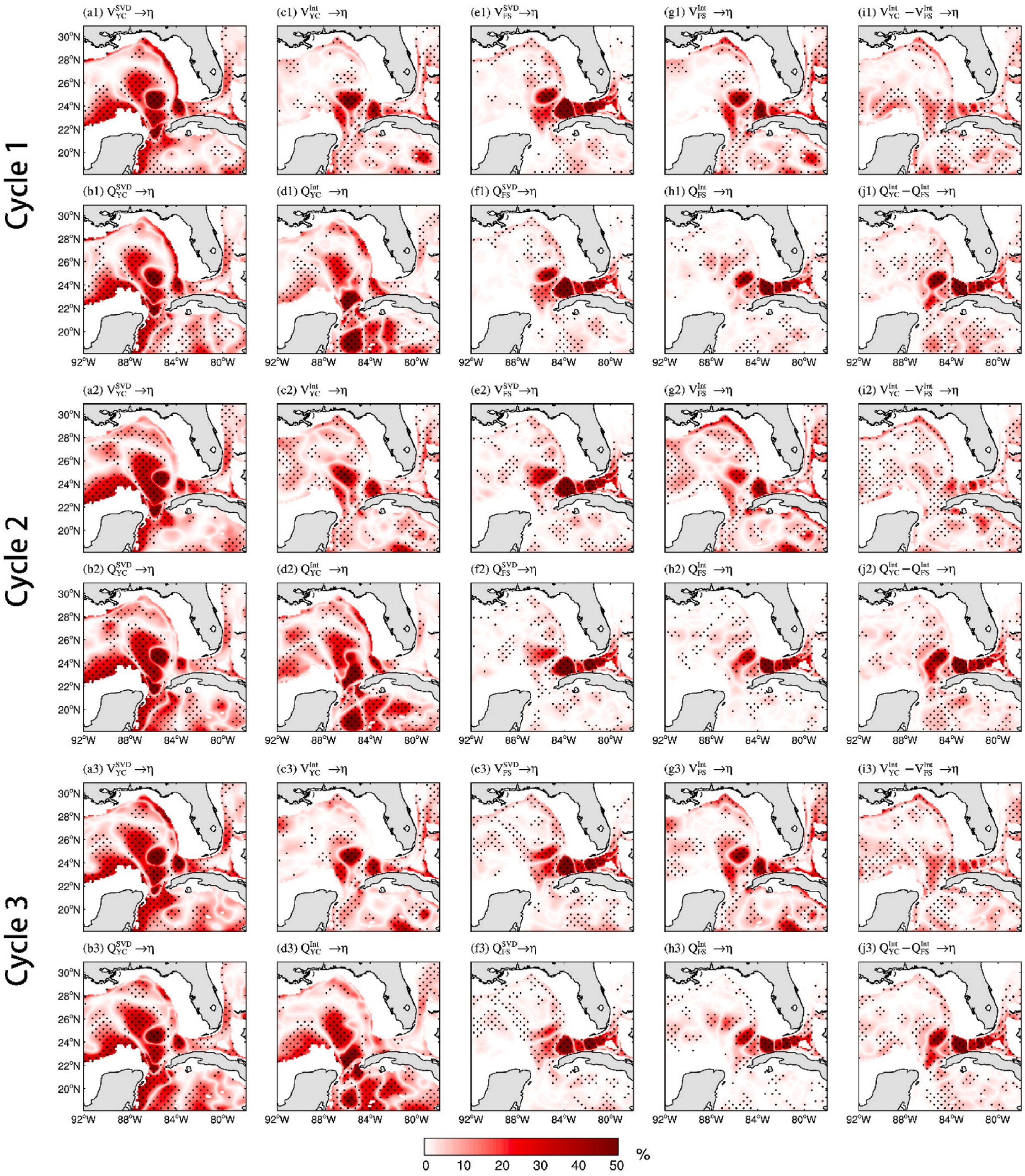

Fig. 11. As in Fig. 8, but for the horizontal casual patterns diagnosed from the three cycles of the HYCOM 54-year experiment.

conditions in the two channels and the LC path state is identified. It is found that the transport and vorticity flux in the two channels cause the LC extension, while the LC path state is less causal to the current variability in the two channels. Spatial structures of the IFs further reveal that the flow variability in the YC has strong influence on the main body of the LC as well as its extension area, while the current variability in the FS mainly influences the eastern branch of the LC. These casual relations obtained from the data-assimilative reanalysis product are further confirmed in a 54-year free-running model simulation, which is repeatedly forced by the same 18-year realistic atmospheric forcing three times. With different initial conditions but identical surface forcings, the LC path variations in the three simulation cycles display substantial differences, indicating a dominance of intrinsic variability in the LC system. Although the strength of the causality varies from one simulation cycle to another, the asymmetric feature of the causality is found robust across the three simulation cycles.

Our causality analysis indicates that both of the transport fluctuations in YC and FS are causal to the LC path variation. In addition, there is also a strong IF from the YC transport to the FS transport. These results indicate that the current variability in YC can affect the LC path in two different ways: one is directly from the YC transport to the LC path, another is first from the YC transport to the FS transport and then from the FS transport to the LC path. Since both ways have strong IFs, they can be both important mechanisms influencing the LC path state.

Finally, we stress that the aim of the present study is to quantify the causal relations between the forcings at the inflow/outflow channels and the LC extension, and hence providing guidance for future studies in this field. From the causal relationships identified in this study, it is

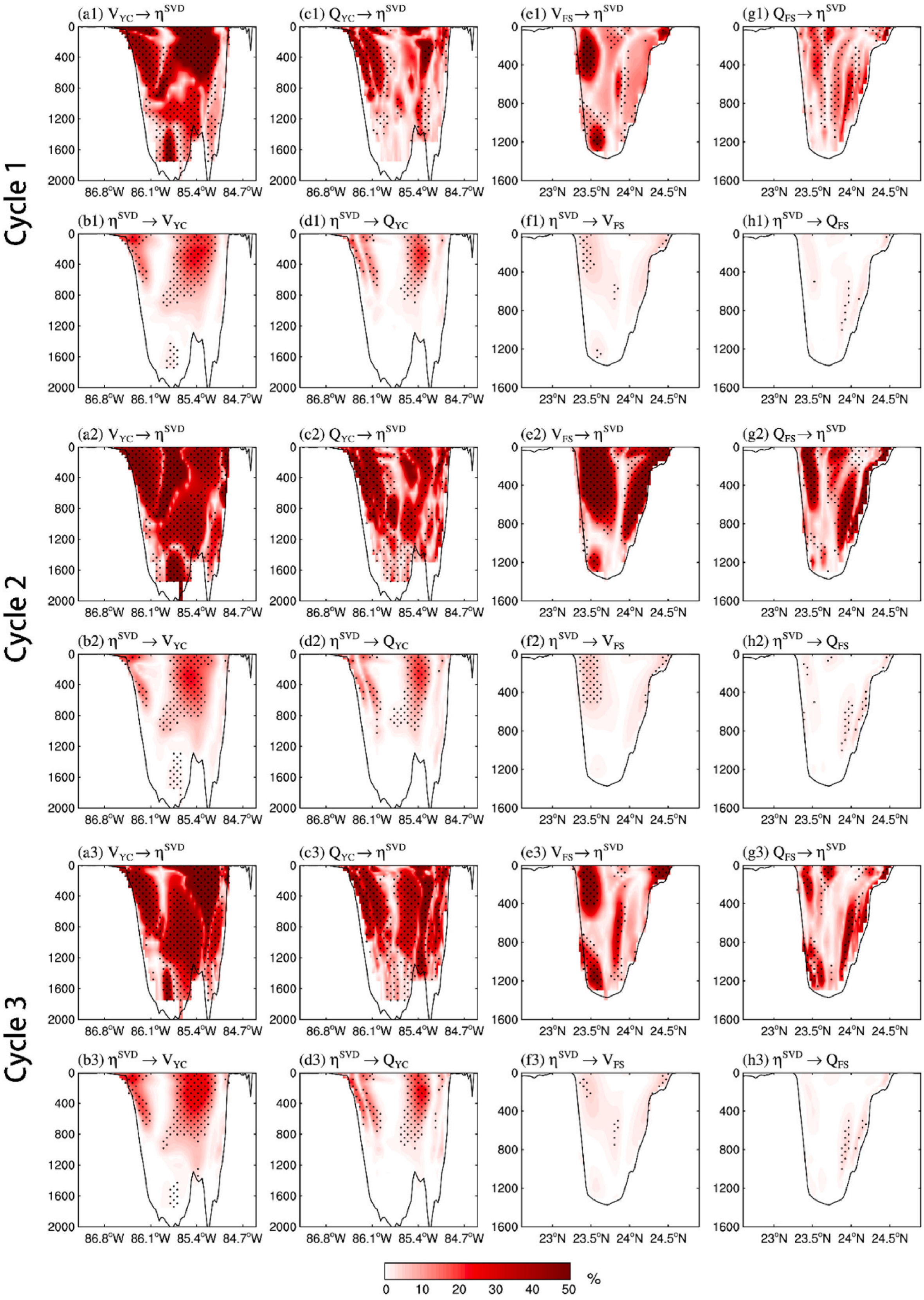

Fig. 12. As in Fig. 9, but for the vertical casual patterns diagnosed from the three cycles of the HYCOM 54-year experiment.

important to implement extensive ocean observations in both inflow and outflow regions, e.g., mooring arrays across the Channel/Straits and High-Frequency Radar networks on Yucatan coast and along the Florida Keys for direct current measurements (e.g., Liu et al., 2021). The dynamics underlying these causal paths, however, remains unclear. Unlike the upstream influence from the entry portal, the downstream-to-upstream scenario occurring between the forcing at the exit portal and the LC is less understood and studied. The forcing may originate from the open ocean (Sturges et al., 2010) and may influence the LC variability through interaction with the West Florida Shelf (Weisberg and Liu, 2017). It is also possible that the outflow could be blocked or allowed by the presence of eddy-like structures that passes through the FS, which in turn impacts the upstream LC. Future efforts are needed to address the mechanism for this intriguing downstream influence.

Author statement

Yang Yang: Conceptualization, Formal analysis, Visualization, Writing - Original Draft, Writing - Review & Editing.

Guanqi Fu: Formal analysis, Visualization.

X. San Liang: Methodology, Writing - Review & Editing.

Robert H. Weisberg: Writing - Review & Editing.

Yonggang Liu: Writing - Review & Editing.

Declaration of competing interest

The authors declare that they have no known competing financial interests or personal relationships that could have appeared to influence the work reported in this paper.

Data availability

I have shared the link to my data in the Acknowledgements

Acknowledgements

We thank the two anonymous referees for their valuable comments. Thanks are also due to Julio Sheinbaum and Julio Candela for providing the CANEK data. The altimetry product is available at https://resources.marine.copernicus.eu. The HYCOM simulation outputs are available at https://www.hycom.org/dataserver. YY and XSL are supported by the National Science Foundation of China (NSFC) under Grant #42276017, 42230105 and 41975064. RHW and YL are partially supported by the Gulf Research Program of the National Academy of Sciences (SCON-10000542) and the NOAA IOOS SECOORA Program (NA21NOS0120097).

References

Alvera-Azcárate, A., Barth, A., Weisberg, R.H., 2009. The surface circulation of the Caribbean Sea and the Gulf of Mexico as inferred from satellite altimetry. J. Phys. Oceanogr. 39, 640–657. https://doi.org/10.1175/2008JPO3765.1.

Athié, G., Sheinbaum, J., Candela, J., Ochoa, J., Pérez-Brunius, P., Romero-Arteaga, A., 2019. Seasonal variability of the transport through the Yucatan Channel from observations. J. Phys. Oceanogr. 50, 343–360. https://doi.org/10.1175/JPO-D-18-0269.1.

Bunge, L., Ochoa, J., Badan, A., Candela, J., Sheinbaum, J., 2002. Deep flows in the Yucatan Channel and their relation to changes in the Loop Current extension. J. Geophys. Res. Oceans 107, 26-1–26-7. https://doi.org/10.1029/2001JC001256.

Candela, J., Ochoa, J., Sheinbaum, J., López, M., Pérez-Brunius, P., Tenreiro, M., Pallàs-Sanz, E., Athié, G., Arriaza-Oliveros, L., 2019. The flow through the Gulf of Mexico. J. Phys. Oceanogr. 49, 1381–1401. https://doi.org/10.1175/JPO-D-18-0189.1.

Candela, J., Sheinbaum, J., Ochoa, J., Badan, A., Leben, R., 2002. The potential vorticity flux through the yucatan Channel and the loop current in the Gulf of Mexico. Geophys. Res. Lett. 29, 16-1–16-4. https://doi.org/10.1029/2002GL015587.

Chang, Y.-L., Oey, L.-Y., 2013. Coupled response of the trade wind, SST gradient, and SST in the Caribbean Sea, and the potential impact on Loop Current's interannual variability. J. Phys. Oceanogr. 43, 1325–1344. https://doi.org/10.1175/JPO-D-12-0183.1.

Chang, Yu-Lin, Oey, L.-Y., 2013. Loop Current growth and eddy shedding using models and observations: numerical process experiments and satellite altimetry data. J. Phys. Oceanogr. 43, 669–689. https://doi.org/10.1175/JPO-D-12-0139.1.

Chérubin, L.M., Morel, Y., Chassignet, E.P., 2006. Loop Current ring shedding: the formation of cyclones and the effect of topography. J. Phys. Oceanogr. 36, 569–591. https://doi.org/10.1175/JPO2871.1.

Cummings, J.A., 2005. Operational multivariate ocean data assimilation. Q. J. R. Meteorol. Soc. 131, 3583–3604. https://doi.org/10.1256/qj.05.105.

Donohue, K.A., Watts, D.R., Hamilton, P., Leben, R., Kennelly, M., 2016. Loop Current Eddy formation and baroclinic instability. Dyn. Atmospheres Oceans, Loop Curr. Dynam. Exper. 76, 195–216. https://doi.org/10.1016/j.dynatmoce.2016.01.004.

Dukhovskoy, D.S., Leben, R.R., Chassignet, E.P., Hall, C.A., Morey, S.L., Nedbor-Gross, R., 2015. Characterization of the uncertainty of loop current metrics using a multidecadal numerical simulation and altimeter observations. Deep-Sea Res. Part A Oceanogr. Res. Pap. 100, 140–158. https://doi.org/10.1016/j.dsr.2015.01.005.

Ezer, T., Oey, L.-Y., Lee, H.-C., Sturges, W., 2003. The variability of currents in the Yucatan Channel: analysis of results from a numerical ocean model. J. Geophys. Res. Oceans 108. https://doi.org/10.1029/2002JC001509.

Garcia Gomez, I., 2020. Intrinsic Ocean Variability Modulated by the Atmosphere in the Gulf of Mexico : an Ensemble Modelling Study.

Granger, C.W.J., 1969. Investigating causal relations by econometric models and cross-spectral methods. Econometrica 37, 424–438. https://doi.org/10.2307/1912791.

Hamilton, P., Lugo-Fernández, A., Sheinbaum, J., 2016. A Loop Current experiment: field and remote measurements. Dyn. Atmospheres Oceans, Loop Curr. Dynam. Exper. 76, 156–173. https://doi.org/10.1016/j.dynatmoce.2016.01.005.

Helber, R.W., Townsend, T.L., Barron, C.N., Dastugue, J.M., Carnes, M.R., 2013. Validation Test Report for the Improved Synthetic Ocean Profile (ISOP) System, Part I: Synthetic Profile Methods and Algorithm. NRL Memo Rep. NRL Memo NRL/MR/7320—13-9364.

Hirschi, J.J.-M., Frajka-Williams, E., Blaker, A.T., Sinha, B., Coward, A., Hyder, P., Biastoch, A., Böning, C., Barnier, B., Penduff, T., Garcia, I., Fransner, F., Madec, G., 2019. Loop Current variability as trigger of coherent Gulf Stream transport anomalies. J. Phys. Oceanogr. 49, 2115–2132. https://doi.org/10.1175/JPO-D-18-0236.1.

Hristopulos, D.T., Babul, A., Babul, S., Brucar, L.R., Virji-Babul, N., 2019. Disrupted information flow in resting-state in adolescents with sports related concussion. Front. Hum. Neurosci. 13.

Huang, M., Liang, X., Zhu, Y., Liu, Y., Weisberg, R.H., 2021. Eddies connect the tropical atlantic ocean and the Gulf of Mexico. Geophys. Res. Lett. 48, e2020GL091277 https://doi.org/10.1029/2020GL091277.

Hurlburt, H.E., Thompson, J.D., 1980. A numerical study of Loop Current intrusions and eddy shedding. J. Phys. Oceanogr. 10, 1611–1651. https://doi.org/10.1175/1520-0485(1980)010<1611:ANSOLC>2.0.CO;2.

Imbens, G.W., Rubin, D.B., 2015. Causal Inference for Statistics, Social, and Biomedical Sciences: an Introduction. Cambridge University Press, Cambridge. https://doi.org/10.1017/CBO9781139025751.

Liang, X.S., 2021. Normalized multivariate time series causality analysis and causal graph reconstruction. Entropy 23, 679. https://doi.org/10.3390/e23060679.

Liang, X.S., 2018. Causation and information flow with respect to relative entropy. Chaos Interdiscip. J. Nonlinear Sci. 28, 075311 https://doi.org/10.1063/1.5010253.

Liang, X.S., 2016. Information flow and causality as rigorous notions ab initio. Phys. Rev. E 94, 052201. https://doi.org/10.1103/PhysRevE.94.052201.

Liang, X.S., 2015. Normalizing the causality between time series. Phys. Rev. E 92, 022126. https://doi.org/10.1103/PhysRevE.92.022126.

Liang, X.S., 2014. Unraveling the cause-effect relation between time series. Phys. Rev. E 90, 052150. https://doi.org/10.1103/PhysRevE.90.052150.

Liang, X.S., 2008. Information flow within stochastic dynamical systems. Phys. Rev. E 78, 031113. https://doi.org/10.1103/PhysRevE.78.031113.

Liang, X.S., Kleeman, R., 2005. Information transfer between dynamical system components. Phys. Rev. Lett. 95, 244101 https://doi.org/10.1103/PhysRevLett.95.244101.

Liang, X.S., Xu, F., Rong, Y., Zhang, R., Tang, X., Zhang, F., 2021. El Niño Modoki can be mostly predicted more than 10 years ahead of time. Sci. Rep. 11, 17860 https://doi.org/10.1038/s41598-021-97111-y.

Lin, Y., Greatbatch, R.J., Sheng, J., 2010. The influence of Gulf of Mexico loop current intrusion on the transport of the Florida current. Ocean Dynam. 60, 1075–1084. https://doi.org/10.1007/s10236-010-0308-0.

Lin, Y., Greatbatch, R.J., Sheng, J., 2009. A model study of the vertically integrated transport variability through the Yucatan Channel: role of Loop Current evolution and flow compensation around Cuba. J. Geophys. Res. Oceans 114. https://doi.org/10.1029/2008JC005199.

Liu, Y., Merz, C.R., Weisberg, R.H., Shay, L.K., Glenn, S.M., Smith, M.J., 2021. An initial evaluation of high-frequency radar radial currents in the Straits of Florida in comparison with altimetry and model products. Ocean Remote Sens. Technol. High Freq. Mar. GNSS-Based Radar 117–144. https://doi.org/10.1049/SBRA537E_ch5.

Liu, Y., Weisberg, R.H., Vignudelli, S., Mitchum, G.T., 2016. Patterns of the loop current system and regions of sea surface height variability in the eastern Gulf of Mexico revealed by the self-organizing maps. J. Geophys. Res. Oceans 121, 2347–2366. https://doi.org/10.1002/2015JC011493.

Lizier, J.T., Prokopenko, M., 2010. Differentiating information transfer and causal effect. Eur. Phys. J. B 73, 605–615. https://doi.org/10.1140/epjb/e2010-00034-5.

Lu, X., Liu, K., Liang, X.S., Lai, K.K., Cui, H., 2022. The dynamic causality in sporadic bursts between CO2 emission allowance prices and clean energy index. Environ. Sci. Pollut. Res. 1–13. https://doi.org/10.1007/s11356-022-21316-5.

Lugo-Fernández, A., 2007. Is the Loop Current a Chaotic Oscillator? J. Phys. Oceanogr. 37, 1455–1469. https://doi.org/10.1175/JPO3066.1.

Lugo-Fernández, A., 2023. A new hypothesis on the intrusion of the Loop Current. Dynam. Atmos. Oceans 102, 101359. https://doi.org/10.1016/j.dynatmoce.2023.101359.

Maul, G.A., 1977. The annual cycle of the Gulf Loop Current, Part 1: observations during a one-year time series. J. Mar. Res. 35, 29–47.

Maul, G.A., Mayer, D.A., Baig, S.R., 1985. Comparisons between a continuous 3-year current-meter observation at the sill of the Yucatan Strait, satellite measurements of Gulf Loop Current area, and regional sea level. J. Geophys. Res. Oceans 90, 9089–9096. https://doi.org/10.1029/JC090iC05p09089.

Maul, G.A., Vukovich, F.M., 1993. The relationship between variations in the Gulf of Mexico Loop Current and Straits of Florida volume transport. J. Phys. Oceanogr. 23, 785–796. https://doi.org/10.1175/1520-0485(1993)023<0785:TRBVIT>2.0.CO;2.

Mildner, T.C., Eden, C., Czeschel, L., 2013. Revisiting the relationship between Loop Current rings and Florida Current transport variability. J. Geophys. Res. Oceans 118, 6648–6657. https://doi.org/10.1002/2013JC009109.

National Academies of Sciences, E., 2018. Understanding and Predicting the Gulf of Mexico Loop Current: Critical Gaps and Recommendations. https://doi.org/10.17226/24823.

Nedbor-Gross, R., Dukhovskoy, D.S., Bourassa, M.A., Morey, S.L., Chassignet, E.P., 2014. Investigation of the relationship between the Yucatan Channel transport and the Loop Current area in a multidecadal numerical simulation. Mar. Technol. Soc. J. 48, 15–26. https://doi.org/10.4031/MTSJ.48.4.8.

Nickerson, A.K., Weisberg, R.H., Liu, Y., 2022. On the evolution of the Gulf of Mexico Loop Current through its penetrative, ring shedding and retracted states. Adv. Space Res. 69, 4058–4077. https://doi.org/10.1016/j.asr.2022.03.039.

Oey, L.-Y., 2004. Vorticity flux through the yucatan Channel and loop current variability in the Gulf of Mexico. J. Geophys. Res. Oceans 109, C10004. https://doi.org/10.1029/2004JC002400.

Oey, L.-Y., Lee, H.-C., Schmitz Jr., W.J., 2003. Effects of winds and Caribbean eddies on the frequency of Loop Current eddy shedding: a numerical model study. J. Geophys. Res. Oceans 108. https://doi.org/10.1029/2002JC001698.

Rosburg, K.C., Donohue, K.A., Chassignet, E.P., 2016. Three-dimensional model-observation comparison in the Loop Current region. Dyn. Atmospheres Oceans, Loop Curr. Dynam. Exper. 76, 283–305. https://doi.org/10.1016/j.dynatmoce.2016.05.001.

Rousset, C., Beal, L.M., 2011. On the seasonal variability of the currents in the Straits of Florida and Yucatan Channel. J. Geophys. Res. Oceans 116. https://doi.org/10.1029/2010JC006679.

Rudnick, D.L., Gopalakrishnan, G., Cornuelle, B.D., 2014. Cyclonic eddies in the Gulf of Mexico: observations by underwater gliders and simulations by numerical model. J. Phys. Oceanogr. 45, 313–326. https://doi.org/10.1175/JPO-D-14-0138.1.

Schmitz, W.J., 2005. Cyclones and westward propagation in the shedding of anticyclonic rings from the Loop Current. In: Sturges, W., Lugo-Fernandez, A. (Eds.), Circulation in the Gulf of Mexico: Observations and Models, Geophys. Monogr. American Geophysical Union, Washington, D. C., pp. 241–261. https://doi.org/10.1029/161GM18

Schreiber, T., 2000. Measuring information transfer. Phys. Rev. Lett. 85, 461–464. https://doi.org/10.1103/PhysRevLett.85.461.

Sheinbaum, J., Athié, G., Candela, J., Ochoa, J., Romero-Arteaga, A., 2016. Structure and variability of the Yucatan and loop currents along the slope and shelf break of the Yucatan channel and Campeche bank. Dyn. Atmospheres Oceans, Loop Curr. Dynam. Exper. 76, 217–239. https://doi.org/10.1016/j.dynatmoce.2016.08.001.

Sheinbaum, J., Candela, J., Badan, A., Ochoa, J., 2002. Flow structure and transport in the Yucatan Channel. Geophys. Res. Lett. 29, 10–11. https://doi.org/10.1029/2001GL013990, 10–4.

Smirnov, D.A., 2013. Spurious causalities with transfer entropy. Phys. Rev. E 87, 042917. https://doi.org/10.1103/PhysRevE.87.042917.

Smith, R.H., Johns, E.M., Goni, G.J., Trinanes, J., Lumpkin, R., Wood, A.M., Kelble, C.R., Cummings, S.R., Lamkin, J.T., Privoznik, S., 2014. Oceanographic conditions in the Gulf of Mexico in july 2010, during the deepwater horizon oil spill. Continent. Shelf Res. 77, 118–131. https://doi.org/10.1016/j.csr.2013.12.009.

Stips, A., Macias, D., Coughlan, C., Garcia-Gorriz, E., Liang, X.S., 2016. On the causal structure between CO2 and global temperature. Sci. Rep. 6, 21691 https://doi.org/10.1038/srep21691.

Stokes, P.A., Purdon, P.L., 2017. A study of problems encountered in Granger causality analysis from a neuroscience perspective. Proc. Natl. Acad. Sci. USA 114, E7063–E7072. https://doi.org/10.1073/pnas.1704663114.

Sturges, W., Hoffmann, N.G., Leben, R.R., 2010. A trigger mechanism for Loop Current ring separations. J. Phys. Oceanogr. 40, 900–913. https://doi.org/10.1175/2009JPO4245.1.

Vastano, J.A., Swinney, H.L., 1988. Information transport in spatiotemporal systems. Phys. Rev. Lett. 60, 1773–1776. https://doi.org/10.1103/PhysRevLett.60.1773.

Weisberg, R.H., Liu, Y., 2017. On the loop current penetration into the Gulf of Mexico. J. Geophys. Res. Oceans 122, 9679–9694. https://doi.org/10.1002/2017JC013330.

Xu, F.-H., Chang, Y.-L., Oey, L.-Y., Hamilton, P., 2013. Loop Current growth and eddy shedding using models and observations: analyses of the July 2011 eddy-shedding event. J. Phys. Oceanogr. 43, 1015–1027. https://doi.org/10.1175/JPO-D-12-0138.1.

Yang, Y., Weisberg, R.H., Liu, Y., Liang, X.S., 2020. Instabilities and multiscale interactions underlying the Loop Current eddy shedding in the Gulf of Mexico. J. Phys. Oceanogr. 50, 1289–1317. https://doi.org/10.1175/JPO-D-19-0202.1.

Yi, B., Bose, S., 2022. Quantum Liang information flow as causation quantifier. Phys. Rev. Lett. 129, 020501 https://doi.org/10.1103/PhysRevLett.129.020501.

Zhang, Y., Hu, C., Liu, Y., Weisberg, R.H., Kourafalou, V.H., 2019. Submesoscale and mesoscale eddies in the Florida Straits: observations from satellite ocean color measurements. Geophys. Res. Lett. 46, 13262–13270. https://doi.org/10.1029/2019GL083999.